

Density and Polarization of Active Brownian Particles in Curved Activity Landscapes

Sven Auschra^{1,*} and Viktor Holubec^{1,2,†}

¹*Institute for Theoretical Physics, Leipzig University, 04103 Leipzig, Germany*

²*Charles University, Faculty of Mathematics and Physics, Department of Macromolecular Physics, V Holešovičkách 2, CZ-180 00 Praha, Czech Republic*

(Dated: May 5, 2021)

Suspensions of motile active particles with space dependent activity form characteristic polarization and density patterns. Recent single-particle studies for planar activity landscapes identified several quantities associated with emergent density-polarization patterns that are solely determined by bulk variables. Naive thermodynamic intuition suggests that these results might hold for arbitrary activity landscapes mediating bulk regions, and thus could be used as benchmarks for simulations and theories. However, the considered system operates in a non-equilibrium steady state, and we prove by construction that the quantities in question lose their simple form for curved activity landscapes. Specifically, we provide a detailed analytical study of polarization and density profiles induced by radially symmetric activity steps, and of the total polarization for the case of a general radially symmetric activity landscape. While the qualitative picture is similar to the planar case, all the investigated variables depend not only on bulk variables but also comprise geometry-induced contributions. We verified that all our analytical results agree with exact numerical calculations.

I. INTRODUCTION

To feed, hide, or proliferate, both macroscopic [1–3] and microscopic [4–8] living organisms actively adjust their motion to mechanical, optical, or chemical stimuli. The ability to change motility based on the state of the environment is also vital for artificial *motile* active matter ranging from robots [9, 10] to microscopic active particles [11–14], where some of the ultimate goals are noninvasive drug delivery and microsurgery [15, 16]. On much lower level of sophistication, large assemblies of active particles exhibit motility-induced phase separation (MIPS) [17] into a dense and slow, and dilute and fast phase [18–20]. Typically but not exclusively, this separation is a consequence of a density dependent propulsion speed [21–24].

The inhomogenous or space dependent activity comes hand in hand with characteristic modulations in the local density and polarization [7, 8, 22, 25–28]. Given the omnipresence of inhomogenous activity at all scales of active matter, the latter can serve as mesoscale indicator for intrinsic microscopic activity in the system [29, 30]. In spite of that, a thorough investigation of characteristic patterns in the local density and polarization attracted a focused attention of the active matter community only recently.

It was shown [29, 30] that density and polarization for a single micrometer-sized Janus swimmer in water are well captured by the active Brownian particle (ABP) model [31–35] for non-interacting active spheres in a noisy environment. For a single-swimmer and a planar activity interface [30], this model allows to identify three quantities that are solely determined by bulk diffusion coefficients, swim speeds, and system size, and thus acquire

the status of thermodynamic state variables. Namely (i) the local polarization peak at the interface, (ii) the ratio of densities of the bulk regions on either side of the interface, and (iii) the total polarization caused by the activity step. The latter two maintain this property irrespective of the shape of the (onedimensional) activity modulations, as long as they mediate between two bulk regions [30, 36]. If generally valid, these simple relations can serve as consistency checks for simulations and benchmarks for theories [36].

In this article, we prove by construction that these results in general do not hold for other than planar activity profiles. Concretely, we applied the theoretical framework of Ref. [30] to radially symmetric activity steps and investigated in detail the resulting polarization and density patterns. Our analytical results show that the quantities (i)–(iii) depend on the non-zero curvature of the interface and thus on the geometry of the setup. We also investigate the (radial) total polarization for general radially symmetric motility modulations and show that it acquires a geometry-induced non-local contribution and hence is no longer determined only by bulk variables. In the limit of vanishing curvature, the obtained results converge to those for planar activity steps [30, 36]. Our theoretical results can be readily tested using the experimental setup used in Ref. [37].

Our results would be surprising for a system in thermodynamic equilibrium with solid walls, where their shape does not affect bulk properties. However, they might be expected for the active-matter system at hand, as it operates in a non-equilibrium steady-state. Indeed, the dependence of bulk properties in active-matter systems on the shape of their physical boundaries has been observed in Refs. [38–41]. The dependence on the interface curvature found here can be compared to the Laplace pressure [42], e.g. in soap bubbles. The main difference between the two setups is that the increased pressure inside a bubble is caused by a physical force applied in the

* sven.auschra@gmail.com

† viktor.holubec@mff.cuni.cz

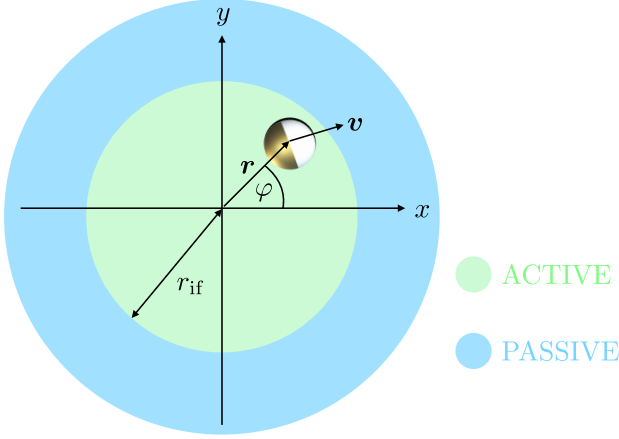


FIG. 1. Janus particle with coordinates $x = r \cos \phi$, $y = r \sin \phi$ subjected to a radially symmetric activity profile. The particle propels actively along its orientation $\mathbf{v}/v = (\cos \theta, \sin \theta)^\top$ for $r \equiv |\mathbf{r}| < r_{\text{if}}$. Otherwise, its swim speed v is zero.

form of the surface tension by the soap film on the bubble interior. The activity interface in our setup is fixed and the observed influence of its curvature can be traced to geometry-induced imbalance of probability currents across the curved interface.

II. THE MODEL

Consider an overdamped Janus swimmer with space dependent propulsion speed (activity) $v(x, y)$ and orientation parametrized by the angle θ confined in a plane. For a piecewise constant radially-symmetric activity profile, we depict the system in Fig. 1. We model the particle dynamics by the Active Brownian particle model [43] described by the system of Langevin equations

$$\partial_t x = v(x, y) \cos \theta + \sqrt{2D} \xi_x, \quad (1)$$

$$\partial_t y = v(x, y) \sin \theta + \sqrt{2D} \xi_y, \quad (2)$$

$$\partial_t \theta = \sqrt{2D_r} \xi_\theta. \quad (3)$$

The translational and rotational diffusion coefficients D and D_r , respectively, measure intensities of independent, unit variance, unbiased Gaussian white noise processes $\xi_{x,y,\theta}(t)$.

In the following section, we utilize the framework of Ref. [30] to derive approximate differential equations for the stationary probability density $\rho(\mathbf{r})$ to find the particle at position \mathbf{r} and the corresponding polarization $\mathbf{p}(\mathbf{r})$.

III. MOMENT EQUATIONS

The dynamic probability density $f(\mathbf{r}, \hat{\mathbf{n}}, t)$ for finding the Janus swimmer at time t at position \mathbf{r} with the orientation $\hat{\mathbf{n}} = (\cos \theta, \sin \theta)^\top$, corresponding to the system of

stochastic differential equations (1)–(3), obeys the FPE [34, 35, 44]

$$\partial_t f = D \nabla^2 f + D_r \partial_\theta^2 f - \nabla \cdot [f v(\mathbf{r}) \hat{\mathbf{n}}]. \quad (4)$$

Here, $\partial_t \equiv \partial/\partial t$, and ∇ represents the Nabla operator with respect to \mathbf{r} . The exact moment expansion of f in terms of $\hat{\mathbf{n}}$ [34, 44, 45] truncated after the second term reads [30]

$$f(\mathbf{r}, \hat{\mathbf{n}}, t) = \frac{1}{2\pi} [\rho(\mathbf{r}, t) + 2\mathbf{p}(\mathbf{r}, t) \cdot \hat{\mathbf{n}}], \quad (5)$$

where

$$\rho(\mathbf{r}, t) \equiv \int d\hat{\mathbf{n}} f(\mathbf{r}, \hat{\mathbf{n}}, t), \quad (6)$$

$$\mathbf{p}(\mathbf{r}, t) \equiv \int d\hat{\mathbf{n}} \hat{\mathbf{n}} f(\mathbf{r}, \hat{\mathbf{n}}, t) \quad (7)$$

denote time-resolved density and polarization, respectively. Multiplying Eq. (4) by 1 or $\hat{\mathbf{n}}$, integrating over orientational degrees of freedom, and using the definitions (6) and (7), we obtain the moment equations [43, 44]

$$\partial_t \rho(\mathbf{r}, t) = -\nabla \cdot \mathbf{J}(\mathbf{r}, t), \quad (8)$$

$$\partial_t \mathbf{p}(\mathbf{r}, t) = -D_r \mathbf{p}(\mathbf{r}, t) - \nabla \cdot \mathbf{M}(\mathbf{r}, t). \quad (9)$$

Here, we introduced the (orientation averaged) flux

$$\mathbf{J}(\mathbf{r}, t) \equiv -D \nabla \rho(\mathbf{r}, t) + v(\mathbf{r}) \mathbf{p}(\mathbf{r}, t), \quad (10)$$

and the matrix flux

$$\mathbf{M}(\mathbf{r}, t) \equiv -D \nabla \mathbf{p}(\mathbf{r}, t) + \frac{v(\mathbf{r})}{2} \rho(\mathbf{r}, t) \mathbf{1}, \quad (11)$$

with the unit matrix $\mathbf{1}$.

Throughout the rest of this article, we will focus on the steady-state solutions $\rho(\mathbf{r})$ and $\mathbf{p}(\mathbf{r})$ of Eqs. (8) and (9), which obey $\partial_t \rho = \partial_t \mathbf{p} = 0$ and thus

$$D \nabla^2 \rho(\mathbf{r}) = \nabla \cdot [v(\mathbf{r}) \mathbf{p}(\mathbf{r})], \quad (12)$$

$$D \nabla^2 \mathbf{p}(\mathbf{r}) = D_r \mathbf{p}(\mathbf{r}) + \frac{1}{2} \nabla [v(\mathbf{r}) \rho(\mathbf{r})]. \quad (13)$$

Moreover, we assume that, under no-flux boundary conditions, the stationary flux $\mathbf{J}(\mathbf{r})$ vanishes. While this assumption is not generally valid in two (or higher) dimensions, it holds for all setups considered below. Exploiting the no-flux condition in Eq. (10) and substituting the resulting formula

$$\nabla \rho(\mathbf{r}) = \frac{v(\mathbf{r})}{D} \mathbf{p}(\mathbf{r}), \quad (14)$$

into Eq. (13), we obtain

$$\nabla^2 \mathbf{p}(\mathbf{r}) = \frac{\mathbf{p}(\mathbf{r})}{\lambda^2(\mathbf{r})} + \frac{\rho(\mathbf{r})}{2D} \nabla v(\mathbf{r}), \quad (15)$$

where we have introduced the length scale

$$\lambda(\mathbf{r}) \equiv \left[\frac{D_r}{D} + \frac{v^2(\mathbf{r})}{2D^2} \right]^{-1/2}. \quad (16)$$

A thorough discussion and physical interpretation of this characteristic length scale in the case of a planar motility step is given in Refs. [29, 30] and we omit it here.

IV. ACTIVE-PASSIVE INTERFACE

We will now solve Eqs. (14) and (15) for ρ and \mathbf{p} for the radially symmetric activity step sketched in Fig. 1. In this setup, the swim speed $v(r) \equiv v_0$, for $r \equiv \sqrt{x^2 + y^2} < r_{\text{if}}$, and is zero otherwise.

Polarization and density must reflect the radial symmetry of the activity profile leading to $\rho = \rho(r)$ and $\mathbf{p} = p(r)\hat{\mathbf{r}}$, where $\hat{\mathbf{r}} \equiv \mathbf{r}/r = (\cos \varphi, \sin \varphi)^\top$. Using this ansatz, the flux-balance condition (14) reduces to

$$\rho'(r) = \frac{v(r)}{D} p(r), \quad (17)$$

where $\rho'(r) \equiv \partial \rho / \partial r$. Exploiting this relation in the moment Eq. (15) yields

$$p''(r) = -\frac{p'(r)}{r} + \frac{p(r)}{r^2} + \frac{p(r)}{\lambda^2(r)} + \frac{v'(r)\rho(r)}{2D}. \quad (18)$$

For the planar setup of Refs. [29, 30] corresponding to $r_{\text{if}} \rightarrow \infty$, the first two terms on the r.h.s. of this equation are zero, which suggests that the polarization and its derivative decay with the distance from the interface faster than $1/r^2$ and $1/r$, respectively. In general, the last term of Eq. (18) vanishes everywhere except for $r = r_{\text{if}}$, since $v'(r) = -v_0\delta(r - r_{\text{if}})$, with the Dirac delta function $\delta(r)$. Within the active ($r \leq r_{\text{if}}$) and passive region ($r > r_{\text{if}}$), Eq. (18) reduces to the modified Bessel equation [7, 8]. Its general solution reads [46]

$$p_{a,p}(r) = C_{a,p}^{(1)} I_1(r/\lambda_{a,p}) + C_{a,p}^{(2)} K_1(r/\lambda_{a,p}), \quad (19)$$

where $I_m(x)$ and $K_m(x)$ are the modified Bessel functions of the first and second kind, respectively. The characteristic length scales

$$\lambda_a \equiv \left(\frac{D_r}{D} + \frac{v_0^2}{2D^2} \right)^{-1/2}, \quad \lambda_p \equiv \left(\frac{D_r}{D} \right)^{-1/2}, \quad (20)$$

follow from Eq. (16) evaluated in the active and passive region, respectively.

In order to create bulk regions with constant density and vanishing polarization both in the active and in the passive region, we demand in the following that the active-passive interface is far enough both from the origin and from the system's boundary at $r = R$. That is, we assume that r_{if} and $R - r_{\text{if}}$ are several times greater than λ_a and λ_p , respectively. This allows us to apply the boundary conditions

$$p_a(r = 0) = 0, \quad p_p(r = R) = 0. \quad (21)$$

Then the general solution (19) simplifies to

$$p(r) = \begin{cases} p_a(r) = C_a I_1(r/\lambda_a) & \text{for } r \leq r_{\text{if}} \\ p_p(r) = C_p K_1(r/\lambda_p) & \text{for } r > r_{\text{if}} \end{cases}. \quad (22)$$

Integration of Eq. (17) delivers the corresponding density

$$\rho(r) = \begin{cases} \rho_a + \frac{v C_a \lambda_a}{D} [I_0(r/\lambda_a) - 1] & \text{for } r \leq r_{\text{if}} \\ \rho_a + \frac{v C_p \lambda_p}{D} [I_0(r_{\text{if}}/\lambda_p) - 1] \equiv \rho_p & \text{for } r > r_{\text{if}} \end{cases}, \quad (23)$$

which assumes the bulk value $\rho_a \equiv \rho(0)$ in the active and $\rho_p \equiv \rho(r_{\text{if}}) \equiv \rho(R)$ in the passive region. The constants C_a and C_p in Eq. (22) can be determined from continuity conditions on p and the corresponding flux \mathbf{M} at the active-passive interface [47]. Demanding the polarization $p(r)$ and the projection

$$\mathbf{M} \cdot \hat{\mathbf{r}} = \left[-D p'(r) + \frac{v(r)\rho(r)}{2} \right] \hat{\mathbf{r}} \quad (24)$$

of the matrix flux (11) onto the radial direction to be continuous at $r = r_{\text{if}}$ renders

$$p_a(r_{\text{if}}) = p_p(r_{\text{if}}), \quad (25)$$

$$p_a'(r_{\text{if}}) - p_p'(r_{\text{if}}) = \frac{v_0}{2D} \rho(r_{\text{if}}). \quad (26)$$

The density (23) satisfies $\rho_a(r_{\text{if}}) = \rho_p(r_{\text{if}})$ by construction. The normal component $\mathbf{J} \cdot \hat{\mathbf{r}}$ is continuous due to the imposed no-flux condition $\mathbf{J} \equiv \mathbf{0}$. The constant ρ_a in Eq. (23) follows from the normalization condition

$$\int_0^{2\pi} d\phi \int_0^R dr \, r \rho(r) = 1. \quad (27)$$

Figures 2 a) and b) show nice agreement of the approximate analytic density and polarization profiles (22) and (23) with exact numerical solutions [48] for two distinct particle activities, expressed in terms of the Péclet number

$$\mathcal{P} \equiv \frac{v_0^2}{2DD_r}. \quad (28)$$

We observe nice agreement with exact numerical solutions [48] in both cases. In Sec. VB, we show that the approximate solutions deviate from the exact results for much smaller Péclet numbers than $\mathcal{P} = 100$ found for straight planar interfaces [49]. This is because Eq. (18) cannot be mapped onto an exactly solvable (2-species) run-and-tumble model [27] providing the same phenomenology as the full model [50], which was the key ingredient for success of the approximate solutions at planar interfaces [29, 30].

The qualitative behavior of density and polarization profiles is the same as for a planar activity step [29, 30]. Namely, an increased activity step induces a higher polarization and a larger ratio ρ_p/ρ_a of bulk densities of the passive and active regions. The polarization peaks exactly at the active-passive interface and decays over characteristic lengths λ_p and $\lambda_a < \lambda_p$ into the passive and active region, respectively. The density profile remains constant at the bulk density $\rho = \rho_p$ throughout

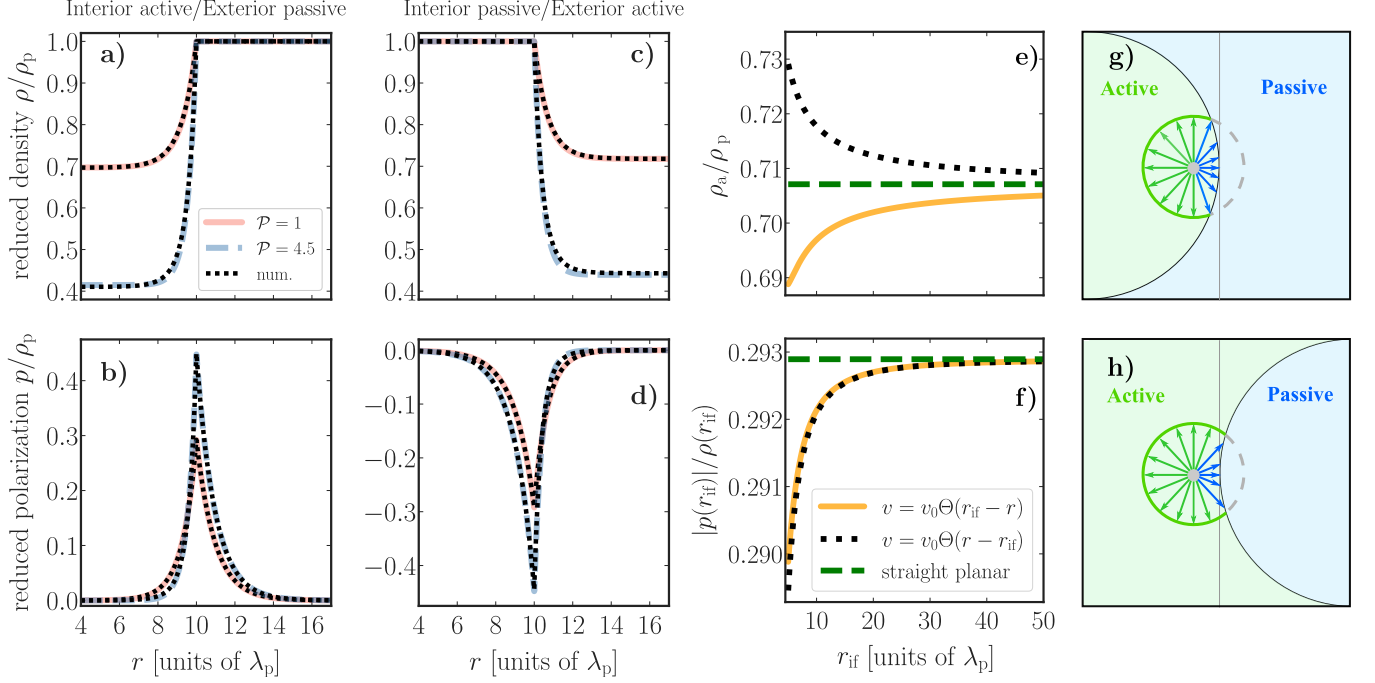


FIG. 2. **a)-d)**: Reduced density (top) and polarization (bottom) profiles near a radially symmetric active-passive [a),b)] / passive-active [c),d)] interface at $r = r_{if}$. Lengths are measured in units of $\lambda_p = \sqrt{D/D_r}$ and velocities in units of $\sqrt{2DD_r}$. This corresponds to a dimensionless theoretical description in terms of the Péclet number \mathcal{P} (28). Theory profiles (solid/dashed curves) were calculated for two distinct \mathcal{P} and $r_{if} = 10 \lambda_p$ using Eqs. (22)-(27) in a) and b) and Eqs. (B1)-(B6) in c) and d), and compared against exact numerically obtained [48] profiles (dotted lines). **e), f)**: Density ratio, ρ_a/ρ_p , and magnitude of the (reduced) polarization at the interface, $|p(r_{if})|/\rho(r_{if})$, for $\mathcal{P} = 1$ as functions of the radial distance r_{if} of the interface. Plotted curves correspond to the following analytical expressions (setups): Solid curves (interior active/exterior passive): Eqs. (29) and (30); Dotted curves (interior passive/exterior active): Eqs. (B8) and (B9); Dashed lines (straight planar case): Eqs. (33) and (35). **g)/ h)**: Particle inside the active region in the vicinity of a concave/convex active-passive interface. In both panels, the vertical line corresponds to a straight active-passive interface. Relative to the latter case, for a concave/convex geometry, the particle has a higher/lower chance to end up in the passive region.

the whole passive region. On crossing the interface, it decays to the bulk density $\rho_a < \rho_p$ pertaining to the active region over a length scale λ_a . We refer to Refs. [29, 30] for a more detailed physical interpretation and discussion of the emerging polarization and density variations. Here, we focus on the influence of curvature on these profiles.

In Figs. 2 c) and d), we show the (reduced) density and polarization profiles corresponding to the inverse setup for which the particle is passive for $r < r_{if}$ and active otherwise. The derivation of the analytic profiles (solid/dashed lines) is similar to the above calculations, and is detailed in App. B. The approximate theory profiles overlap with the corresponding exact numerical solutions. The qualitative picture is similar to the situation shown in Figs. 2 a) and b), with flipped active/passive regions, and a negative polarization in the vicinity of the interface, confirming that the particle preferably points into the passive region [29, 30]. Note, however, that the convexity/concavity of the activity interface also leads to quantitative differences between the two cases.

To grasp the influence of the curvature of the activity step more quantitatively, we compare the maximum relative polarization, $p(r_{if})/\rho(r_{if})$, which constitutes a suit-

able order parameter for the polarization at the interface, and the bulk density ratio, ρ_a/ρ_p , for circular and straight planar interfaces. For the setup where the particle is active for $r < r_{if}$ and passive otherwise [Fig. 2 a),b)], these quantities are given by

$$\frac{p(r_{if})}{\rho(r_{if})} = \frac{v_0}{2D} G_A(r_{if}), \quad (29)$$

$$\frac{\rho_a}{\rho_p} = 1 - \frac{v_0^2 \lambda_a}{2D^2} G_A(r_{if}) \left(\frac{I_0}{I_1} - \frac{1}{I_1} \right), \quad (30)$$

as detailed in App. A. Here, the (geometry) function reads

$$G_A(r_{if}) \equiv \left(\frac{I_0 + I_2}{2\lambda_a I_1} + \frac{K_0 + K_2}{2\lambda_p K_1} \right)^{-1}, \quad (31)$$

with $I_m \equiv I_m(r_{if}/\lambda_a)$ and $K_m \equiv K_m(r_{if}/\lambda_p)$. The subscript “A” indicates that G_A corresponds to the case where the particle is *active* for $r < r_{if}$. The geometry function $G_P(r_{if})$ for the inverted setup is derived in App. B. Exploiting the asymptotic expansions $I_n(z) \sim$

$e^z/\sqrt{2\pi z}$ and $K_n(z) \sim e^{-z}/\sqrt{2z/\pi}$, valid for $z \gg 1$ irrespective of the order n [46], one finds

$$G_A(r_{\text{if}}) \sim \frac{\lambda_a \lambda_p}{\lambda_a + \lambda_p}. \quad (32)$$

For $r_{\text{if}} \gg \lambda_p > \lambda_a$, the maximum (relative) polarization therefore approaches

$$\frac{p(r_{\text{if}})}{\rho(r_{\text{if}})} \sim \frac{v_0}{2D} \frac{\lambda_a \lambda_p}{\lambda_a + \lambda_p} = \frac{1}{\sqrt{2}} \frac{\sqrt{\mathcal{P}}}{1 + \sqrt{1 + \mathcal{P}}}, \quad (33)$$

which coincides with the expression found for planar interfaces [30]. The corresponding asymptotic behavior of the density ratio (30)

$$\frac{\rho_a}{\rho_p} \sim 1 - \frac{v_0^2 \lambda_a}{2D^2} \frac{\lambda_a \lambda_p}{\lambda_a + \lambda_p} \left(1 - \sqrt{\frac{2\pi r_{\text{if}}}{\lambda_a}} e^{-r_{\text{if}}/\lambda_a} \right) \quad (34)$$

still displays an exponential decaying with r_{if} . By taking the limit $r_{\text{if}} \rightarrow \infty$, it reduces to the result found at planar activity steps [30]

$$\frac{\rho_a}{\rho_p} = \frac{\lambda_a}{\lambda_p} = \frac{1}{\sqrt{1 + \mathcal{P}}}. \quad (35)$$

The analytic expressions for $p(r_{\text{if}})/\rho(r_{\text{if}})$ and ρ_a/ρ_p for the inverted setup [Fig. 2 c),d)] are derived in App. B along similar lines.

Figures 2 e) and f) show the dependence of these quantities on the radius of curvature r_{if} of the interface for both circular setups, as well as their counterparts (33) and (35) for straight planar interfaces (dashed horizontal lines). With increasing r_{if} , the polarization peaks $|p(r_{\text{if}})|/\rho(r_{\text{if}})$ for the circular setups approach the one for the straight motility step from below. For the setup where the particle is active for $r < r_{\text{if}}$ (solid curve), the peak is slightly larger ($\approx 0.02\%$ for $r_{\text{if}} = 10 \lambda_p$) than for the inverted setup (dotted curve). Turning to the bulk density ratio, if the interior is active (solid line), the bulk density ratio ρ_a/ρ_p is smaller as compared to the straight planar case, whereas it exceeds it for the inverse circular setup (dotted curve).

This behavior can be intuitively understood as a result of a geometry-induced imbalance in probability fluxes across the curved interface. Consider the situations sketched in Fig. 2 g) and h). In both panels, a Janus particle (gray dot) is situated inside an active region, in a close proximity to an adjacent passive region. In g), the active-passive interface is concave, whereas in h), it is convex. In both panels, the vertical lines correspond to a straight active-passive interface. For simplicity, consider a quasi-ballistic particle motion denoted by the arrows in both panels. As indicated by the number of blue arrows relative to the green ones, the particle's chance to enter the passive region is higher for the concave [g)] than convex [h)] geometry. The setup with active interior [g)] thus yields a larger bulk density ratio ρ_a/ρ_p than the inverse setup [h)]. It follows that the density ratio corresponding to a concave/convex active-passive interface is

always smaller/larger than its counterpart for a straight planar interface. As the curvature of the circular activity interface decreases, i.e. for $r_{\text{if}} \rightarrow \infty$, the bulk density ratio for straight interfaces is approached.

To gain an intuition on why the magnitude of the reduced polarization, $|p(r_{\text{if}})|/\rho(r_{\text{if}})$, is always larger in the straight planar case than for a circular interface [see Fig. 2 f)] is more difficult. The absolute value of the polarization $|p(r_{\text{if}})|$ depends on the probability that the particle with a given orientation hits the interface. Compared to the planar case, for the concave interface shown in g), there are less active particles in the bulk to hit the interface with a broader range of polarizations, and vice versa for the convex interface shown in h). Hence we observe three competing ingredients that determine the absolute polarization in the concave (convex) case: low (high) bulk density in the active region, large (small) probability for a given particle to hit the interface, and large (small) average polarization of particles which hit the interface, where the strength of the individual ingredients is compared to the planar case. Furthermore, the magnitude of the reduced polarization is obtained as absolute polarization divided by density of the passive bulk, which is high for the concave and low for the convex case. We thus find in both circular setups two ingredients leading to an increase and two leading to a decrease of $|p(r_{\text{if}})|/\rho(r_{\text{if}})$. Our analytical results show that they compensate each other in such a way that the magnitude of the reduced polarization for circular interfaces is always lower than in the planar case. Unfortunately, it seems impossible to guess the influence of these ingredients based on physical intuition.

The maximum polarization and density ratios, which are for planar motility steps solely determined by bulk variables (v_0, D, D_r) [29, 30] thus depend on the interface radius r_{if} in case of a circular activity step. This suggests that arbitrarily curved activity steps generally yield geometry-induced contributions to the emergent density-polarization patterns, and the corresponding maximum polarization and bulk density ratio. To provide further evidence for this conjecture, we now study the total polarization, which is also solely determined by bulk quantities in the case of planar interfaces [36], for arbitrary radially symmetric activity modulations.

V. TOTAL POLARIZATION

Without alignment forces, local polarization in active-matter systems arises from spacial sorting of particles with different orientations. Therefore the total polarization vector, \mathcal{P}_{tot} , defined as the integral

$$\mathcal{P}_{\text{tot}} \equiv \int_{\mathcal{V}} d\mathbf{r} \, \mathbf{p}(\mathbf{r}) \quad (36)$$

over the whole space \mathcal{V} , universally vanishes for systems with no-flux boundary conditions [36].

A more appropriate definition of total polarization induced by activity landscapes that mediate between two bulk regions is to restrict the domain of integration \mathcal{V} so that it connects the two bulk regions. For planar activity profiles, it is natural to integrate along a ray of fixed width parallel to the x-axis and thus perpendicular to the interface. Then, the magnitude P_{tot} of such defined total polarization is proportional to the difference in strengths of fluxes, $v\rho$, corresponding to the two bulk regions [29, 30], and thus it acquires the status of a thermodynamic state variable. For an arbitrary radial activity profile $v(r)$ that mediates between two bulk regions of respectively constant activity, the radial symmetry implies that the local polarization profile must be of the form $\mathbf{p} = p(r)\hat{\mathbf{r}}$, with $\hat{\mathbf{r}} = (\cos\phi, \sin\phi)^\top$. To match the planar definition, we define the magnitude of the total radial polarization as the integral

$$P_{\text{tot}} \equiv \int_{R_1}^{R_2} dr p(r), \quad (37)$$

of the projection $p(r)$ of the polarization vector onto the radial axis over a ray of fixed infinitesimal width, perpendicular to the interface, and mediating the inner bulk region at radius R_1 and the outer one at R_2 (see Fig. 3). Alternatively, and more naturally from the point of view of polar coordinates, one could integrate the polarization over an infinitesimal wedge mediating the two bulks. This would correspond to substituting $rp(r)$ for $p(r)$ in the definition (37). However, in this case, the width of the integration region increases with r .

Below we show that P_{tot} is generally composed of a contribution proportional to the difference $v(R_1)\rho(R_1) - v(R_2)\rho(R_2)$ of the flux strengths, as for planar interfaces [36], and a second non-local contribution induced by the non-zero curvature of the interface. A similar expression also holds for the alternative definition of P_{tot} with $rp(r)$.

A. Derivation of total polarization

We introduce polar coordinates, $x = r \cos\phi$ and $y = r \sin\phi$, and the angular variable $\psi \equiv \theta - \phi$, which measures the particle orientation relative to the radial axis (see Fig. 3). Under this transformation, the system of three Langevin equations (1)-(3) reduces to the two-dimensional set

$$\partial_t r = v(r) \cos\psi + \sqrt{2D}\xi_r, \quad (38)$$

$$\partial_t \psi = -\frac{v(r)}{r} \sin\psi + \sqrt{2\left(\frac{D}{r^2} + D_r\right)}\xi_\psi, \quad (39)$$

where ξ_r and ξ_ψ denote independent, zero-mean, unbiased Gaussian white noise processes. The associated FPE for the stationary probability density $\mathbf{f}(r, \psi)$ for finding

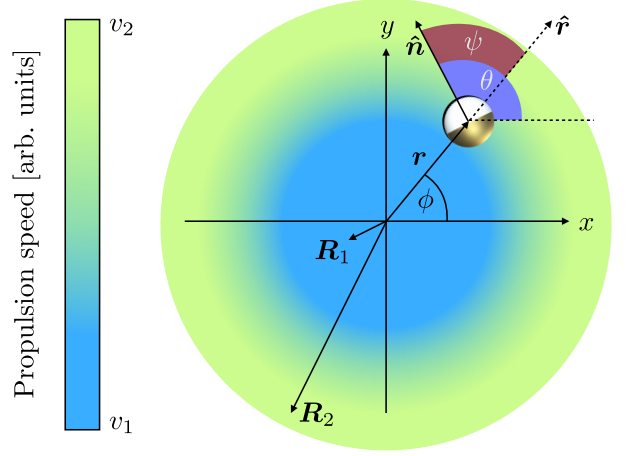


FIG. 3. A Janus particle at position $\mathbf{r} = (r \cos\phi, r \sin\phi)^\top$ actively propelling along its orientation $\hat{\mathbf{n}} = (\cos\theta, \sin\theta)^\top$. The particle's orientation relative to the radial unit vector $\hat{\mathbf{r}}$ is measured by the angle ψ . The swimmer's propulsion speed follows a radially symmetric activity profile (color-coded), which mediates between an inner (dark blue, \mathbf{R}_1) and outer (light green, \mathbf{R}_2) bulk region with different constant activities.

the particle at distance r with relative orientation ψ reads

$$0 = -\partial_r \mathfrak{J} + \left(\frac{D}{r^2} + D_r\right) \partial_\psi^2 \mathfrak{f} + \frac{v(r)}{r} \partial_\psi (\sin\psi \mathfrak{f}), \quad (40)$$

where we have introduced the (angle-resolved) flux

$$\mathfrak{J}(r, \psi) \equiv -D \partial_r \mathfrak{f} + \frac{D}{r} \mathfrak{f} + \cos\psi v(r) \mathfrak{f}. \quad (41)$$

Due to the radial symmetry, \mathfrak{f} and \mathfrak{J} must be even functions of ψ , i.e., $\mathfrak{f}(r, \psi) = \mathfrak{f}(r, -\psi)$, and $\mathfrak{J}(r, \psi) = \mathfrak{J}(r, -\psi)$. The Fourier expansion of the flux \mathfrak{J} thus reads

$$\mathfrak{J}(r, \psi) = \sum_{n=0}^{\infty} \mathfrak{J}_n(r) \cos(n\psi), \quad (42)$$

where $\mathfrak{J}_n(r)$ is the n th Fourier coefficient. Plugging this series into the FPE (40) and integrating twice over the angle from 0 to ψ yields

$$\begin{aligned} \left(\frac{D}{r^2} + D_r\right) \mathfrak{f}(r, \psi) &= \mathfrak{f}_0(r) - \sum_{n=1}^{\infty} \partial_r \mathfrak{J}_n(r) \frac{\cos(n\psi)}{n^2} \\ &\quad - \frac{v(r)}{r} \int_0^\psi d\tilde{\psi} \sin\tilde{\psi} \mathfrak{f}(r, \tilde{\psi}). \end{aligned} \quad (43)$$

The unknown function $\mathfrak{f}_0(r)$ stems from the second integration. The integration constant from the first integration renders, after the second integration, a term linear in ψ , and thus it must be zero to maintain periodicity.

The radial component of the local polarization vector $\mathbf{p}(r)$ is defined by

$$\mathbf{p}(r) \equiv \int_0^{2\pi} d\psi \cos\psi \mathfrak{f}(r, \psi). \quad (44)$$

The corresponding tangential component $\int_0^{2\pi} d\psi \sin \psi \mathbf{f}(r, \psi)$ vanishes due to the radial symmetry. Multiplying Eq. (43) by $\cos \psi$, integrating over ψ from 0 to 2π , and using orthogonality of trigonometric functions renders

$$\left(\frac{D}{r^2} + D_r\right) \mathbf{p}(r) = -\pi \partial_r \mathfrak{J}_1(r) + \frac{v(r)}{r} \int_0^{2\pi} d\psi \sin^2 \psi \mathbf{f}(r, \psi). \quad (45)$$

The integral on the r.h.s. was obtained by interchanging the order of the double integration [51]. Using the definitions (41) and (44), we find that the first coefficient \mathfrak{J}_1 of the Fourier series (42) in terms of \mathbf{f} and \mathbf{p} reads

$$\mathfrak{J}_1 = \frac{1}{\pi} \int_0^{2\pi} d\psi \mathfrak{J}(r, \psi) \cos \psi \quad (46)$$

$$= \frac{1}{\pi} \left(\frac{D}{r} \mathbf{p} - D \partial_r \mathbf{p} \right) + \frac{v}{\pi} \int_0^{2\pi} d\psi \mathbf{f}(r, \psi) \cos^2 \psi. \quad (47)$$

The distributions \mathbf{f} and f and the corresponding polarizations \mathbf{p} and p are connected via the Jacobian [47] $|\partial(x, y)/\partial(r, \phi)| = r$, i.e., $\mathbf{f} = r\mathbf{f}$ and $\mathbf{p} = r\mathbf{p}$. Plugging these transformations and Eq. (47) into Eq. (45) yields

$$D_r p = D \partial_r \left(\frac{p}{r} + \partial_r p \right) - \partial_r (v \langle \cos^2 \psi \rangle) - \frac{v}{r} \langle 2 \cos^2 \psi - 1 \rangle. \quad (48)$$

Here, the averaging is defined as

$$\langle \bullet \rangle \equiv \int_0^{2\pi} d\psi \bullet f(r, \psi). \quad (49)$$

Finally, Eqs. (37) and $2 \cos^2 \psi - 1 = \cos(2\psi)$ render the closed expression for the total polarization:

$$P_{\text{tot}} = \frac{D}{D_r} \left(\frac{p}{r} + \partial_r p \right) \Big|_{R_1}^{R_2} - \frac{v}{D_r} \langle \cos^2 \psi \rangle \Big|_{R_1}^{R_2} - \mathcal{I}[v](R_1, R_2), \quad (50)$$

where we introduced the functional

$$\mathcal{I}[v](R_1, R_2) \equiv \int_{R_1}^{R_2} dr \frac{v(r)}{r D_r} \langle \cos(2\psi) \rangle. \quad (51)$$

Within bulk regions, we have $p(R_{1/2}) = \partial_r p(R_{1/2}) = 0$ and $f(R_{1/2}, \psi) = \rho(R_{1/2})/(2\pi)$. Hence, the first term on the r.h.s. of Eq. (50) vanishes and the second one simplifies to $\langle \cos^2 \psi \rangle(R_{1/2}) = \rho(R_{1/2})/2$. The total polarization between two bulk regions thus reads

$$P_{\text{tot}} = \frac{v(R_1)\rho(R_1) - v(R_2)\rho(R_2)}{2D_r} - \mathcal{I}[v](R). \quad (52)$$

The first summand above coincides with the total polarization found for planar interfaces [29, 30]. The second

term is a non-local contribution attributed to the non-zero curvature of the considered activity profile. It vanishes when the activity profile becomes effectively planar, i.e. when its radius diverges while the thickness measured by the distance between the two bulk regions remains finite. The (radial) total polarization for curved activity profiles is thus not solely determined by stationary properties of the bulk, and, in this sense, loses its status of a state variable. Using Eq. (45), one can show along similar lines as above that a similar expression would be obtained for the alternative definition of the total polarization using \mathbf{p} instead of p in Eq. (37). Specifically, the first term in this total polarization follows from Eq. (52) after substituting $r\rho$ for ρ in the first term on the r.h.s. The curvature dependent term changes more but also vanishes for diverging radius of the interface.

We now demonstrate that $\mathcal{I}[v](R_1, R_2)$ in Eq. (52) vanishes when truncating the exact moment expansion of $f(r, \psi)$ after two terms as in Eq. (5) and quantify deviations between the exact solution and approximate solution of Sec. III.

B. Approximate global sum rule and deviations

Plugging $\rho = \rho(r)$ and $\mathbf{p} = p(r)\hat{\mathbf{r}}$ in to the truncated moment expansion (5), the approximate distribution function can be written as

$$f(r, \psi) = \frac{1}{2\pi} [\rho(r) + p(r) \cos \psi]. \quad (53)$$

Using the average (49), the density $\rho(r)$ and polarization $p(r)$ are given by $\langle 1 \rangle$ and $\langle \cos \psi \rangle$, respectively. All higher (angular) moments within the approximation (53) vanish. In particular, $\langle \cos(2\psi) \rangle = 0$ and the functional \mathcal{I} (51) gives zero. The total polarization (52) then reads

$$P_{\text{tot}} = \frac{v(R_1)\rho(R_1) - v(R_2)\rho(R_2)}{2D_r}, \quad (54)$$

which is the result found for onedimensional activity landscapes [30, 36]. For the radial activity profiles considered here, it only holds within the approximation $\langle \cos(n\psi) \rangle = 0$ for $n > 1$.

To verify the exact analytical result (52) for the total polarization, and to assess the scope of the approximation (54), we numerically calculated the exact distributions $f(r, \psi)$ [48] for several radially symmetric activity steps. As in Sec. IV, the particle propels actively if its radial distance $r < r_{\text{if}}$ and its swimming mechanism is switched off otherwise (see Fig. 1).

The upper panel of Fig. 4 depicts the moments $\langle \cos(n\psi) \rangle$, $n = 0, 1, 2$ calculated from Eq. (49) using the exact distribution $f(r, \psi)$ for Péclet number $\mathcal{P} = 40$. The moments are normalized by the bulk density ρ_a in the active region. In the active region, the second moment $\langle \cos(2\psi) \rangle$ is up to the active-passive interface largely negative rendering its contribution (51) to the total polariza-

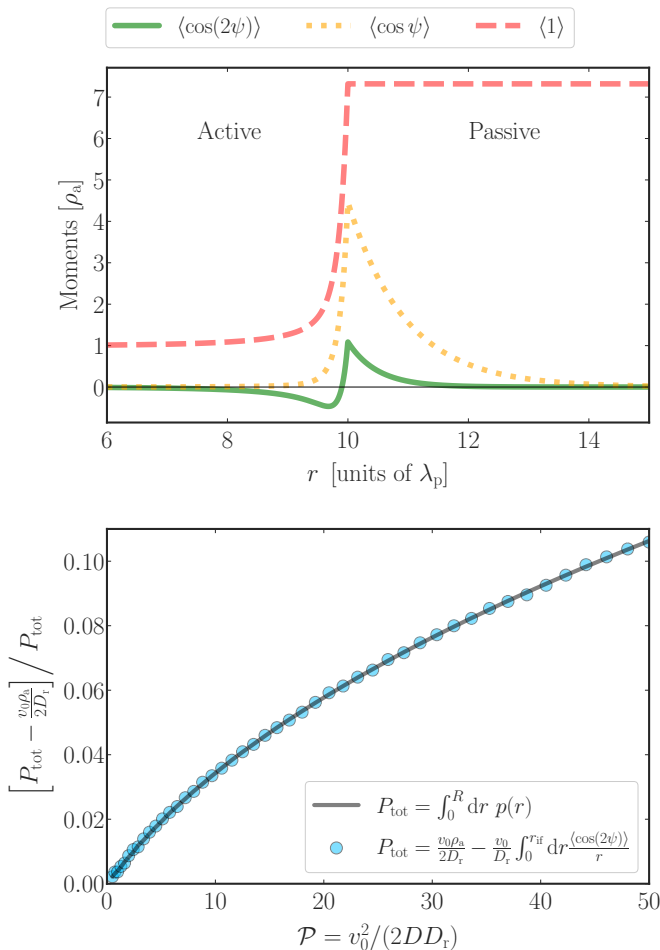


FIG. 4. Moments (Eq. (49), top) and relative deviations of the total polarization (Eq. (37), bottom) from its approximate value (54) in the vicinity of a radially symmetric active-passive interface at $r = r_{\text{if}} = 10 \lambda_p$. The particle propels actively if its radial distance $r < r_{\text{if}}$ and only diffuses otherwise. Lengths are measured in units of $\lambda_p = \sqrt{D/D_r}$ and velocities in units of $\sqrt{2DD_r}$. The overall radial extension of the system was chosen $R = 20 \lambda_p$, and in the top figure we took the Péclet number $\mathcal{P} = v_0 / (2DD_r) = 40$. The presented data was obtained using the exact numerically determined distribution $f(r, \psi)$ [48]. The solid line and circles in the bottom panel were determined from Eqs. (37) and (52), respectively.

tion (52) positive. Since the amplitude of the second mo-

ment increases with Péclet number, the approximate result for the total polarization (54) underestimates its exact value the more the larger the particle activity, as can be inferred from the lower panel of Fig. 4. It shows that the relative deviation between the two reaches roughly 10% for $\mathcal{P} = 50$ and thus the approximation (54) is reasonably accurate for experimentally realizable Péclet numbers [29]. The lower panel of Fig. 4 also shows perfect agreement between the analytical result (52) and polarization evaluated from Eq. (37) using the numerically determined density $f(r, \psi)$.

VI. CONCLUSION

We derived approximate analytical formulas for polarization and density profiles induced by a radially symmetric motility step. These results nicely agree with numerically determined exact solutions even beyond the limit of small activities. We further evaluated the effect of non-zero curvature of the active-passive interface on the polarization and density. Reduced polarization is smaller than for planar activity steps, whereas the contrast in the bulk densities is smaller/larger for concave/convex active-passive interfaces. Both the maximum polarization and the bulk density ratio depend on the curvature of the interface.

Furthermore, we derived an exact formula for the (radial) total polarization induced by an arbitrary radially symmetric activity landscape. Compared to the result for onedimensional activity landscapes, the total polarization contains a non-local, geometry-induced correction. The total polarization is thus no longer determined solely by bulk variables. This result proves that curved active/passive interfaces generally yield a geometry-induced contribution to the emergent density and polarization profiles, and the associated total polarization and bulk density ratio.

ACKNOWLEDGEMENTS

We thank Klaus Kroy for valuable discussions. We acknowledge funding by the Deutsche Forschungsgemeinschaft (DFG) through the priority program “Microswimmers” (SPP 1726, project 237143019), and by Czech Science Foundation (project No. 20-02955J). Viktor Holubec gratefully acknowledges support by the Humboldt foundation.

[1] N. Uchida, A. Kepecs, and Z. F. Mainen, Seeing at a glance, smelling in a whiff: rapid forms of perceptual decision making, *Nature Reviews Neuroscience* **7**, 485 (2006).
[2] S. Sponberg, The emergent physics of animal locomotion, *Physics Today* **70**, 34–40 (2017).

[3] B. Moullia, C. Coutand, and J.-L. Julien, Mechanosensitive control of plant growth: bearing the load, sensing, transducing, and responding, *Frontiers in Plant Science* **6**, 52 (2015).
[4] U. B. Kaupp, J. Solzin, E. Hildebrand, J. E. Brown, A. Helbig, V. Hagen, M. Beyermann, F. Pampaloni, and I. Weyand, The signal flow and motor response control-

- ing chemotaxis of sea urchin sperm, *Nature Cell Biology* **5**, 109–117 (2003).
- [5] B. M. Friedrich and F. Jülicher, Chemotaxis of sperm cells, *Proceedings of the National Academy of Sciences* **104**, 13256–13261 (2007).
 - [6] M. B. Miller and B. L. Bassler, Quorum sensing in bacteria, *Annual Review of Microbiology* **55**, 165–199 (2001).
 - [7] A. Fischer, F. Schmid, and T. Speck, Quorum-sensing active particles with discontinuous motility, *Physical Review E* **101**, 012601 (2020).
 - [8] A. Fischer, F. Schmid, and T. Speck, Erratum: Quorum-sensing active particles with discontinuous motility [phys. rev. e 101, 012601 (2020)], *Physical Review E* **102**, 059903(E) (2020).
 - [9] M. Mijalkov, A. McDaniel, J. Wehr, and G. Volpe, Engineering sensorial delay to control phototaxis and emergent collective behaviors, *Physical Review X* **6**, 011008 (2016).
 - [10] C. Virág, G. Vászrhelyi, N. Tarcai, T. Szörényi, G. Somorjai, T. Nepusz, and T. Vicsek, Flocking algorithm for autonomous flying robots, *Bioinspiration & Biomimetics* **9**, 025012 (2014).
 - [11] J. Anderson, Colloid Transport By Interfacial Forces, *Annual Review of Fluid Mechanics* **21**, 61 (1989).
 - [12] W. Poon, From clarkia to escherichia and janus: The physics of natural and synthetic active colloids, *Proceedings of the International School of Physics "Enrico Fermi"* **184**, 317–386 (2013).
 - [13] A. Zöttl and H. Stark, Emergent behavior in active colloids, *Journal of Physics: Condensed Matter* **28**, 253001 (2016).
 - [14] C. Bechinger, R. Di Leonardo, H. Löwen, C. Reichhardt, G. Volpe, and G. Volpe, Active Particles in Complex and Crowded Environments, *Reviews of Modern Physics* **88**, 045006 (2016).
 - [15] D. Patra, S. Sengupta, W. Duan, H. Zhang, R. Pavlick, and A. Sen, Intelligent, self-powered, drug delivery systems, *Nanoscale* **5**, 1273–1283 (2013).
 - [16] A. Vikram Singh and M. Sitti, Targeted drug delivery and imaging using mobile milli/microrobots: A promising future towards theranostic pharmaceutical design, *Current Pharmaceutical Design* **22**, 1418 (2016).
 - [17] M. E. Cates and J. Tailleur, Motility-induced phase separation, *Annual Review of Condensed Matter Physics* **6**, 219–244 (2015).
 - [18] Y. Fily and M. C. Marchetti, Athermal phase separation of self-propelled particles with no alignment, *Physical Review Letters* **108**, 235702 (2012).
 - [19] I. Buttinoni, J. Bialké, F. Kümmel, H. Löwen, C. Bechinger, and T. Speck, Dynamical clustering and phase separation in suspensions of self-propelled colloidal particles, *Physical Review Letters* **110**, 238301 (2013).
 - [20] G. S. Redner, M. F. Hagan, and A. Baskaran, Structure and dynamics of a phase-separating active colloidal fluid, *Physical Review Letters* **110**, 055701 (2013).
 - [21] A. P. Solon, J. Stenhammar, M. E. Cates, Y. Kafri, and J. Tailleur, Generalized thermodynamics of phase equilibria in scalar active matter, *Physical Review E* **97**, 020602(R) (2018).
 - [22] A. P. Solon, J. Stenhammar, M. E. Cates, Y. Kafri, and J. Tailleur, Generalized thermodynamics of motility-induced phase separation: phase equilibria, laplace pressure, and change of ensembles, *New Journal of Physics* **20**, 075001 (2018).
 - [23] J. Bialké, H. Löwen, and T. Speck, Microscopic theory for the phase separation of self-propelled repulsive disks, *EPL (Europhysics Letters)* **103**, 30008 (2013).
 - [24] T. Speck, A. M. Menzel, J. Bialké, and H. Löwen, Dynamical mean-field theory and weakly non-linear analysis for the phase separation of active brownian particles, *The Journal of Chemical Physics* **142**, 224109 (2015).
 - [25] M. J. Schnitzer, Theory of continuum random walks and application to chemotaxis, *Physical Review E* **48**, 2553 (1993).
 - [26] A. Sharma and J. M. Brader, Brownian systems with spatially inhomogeneous activity, *Physical Review E* **96**, 032604 (2017).
 - [27] K. Malakar, V. Jemseena, A. Kundu, K. Vijay Kumar, S. Sabhapandit, S. N. Majumdar, S. Redner, and A. Dhar, Steady state, relaxation and first-passage properties of a run-and-tumble particle in one-dimension, *Journal of Statistical Mechanics: Theory and Experiment* **2018**, 043215 (2018).
 - [28] S. Hermann, P. Krinninger, D. de las Heras, and M. Schmidt, Phase coexistence of active brownian particles, *Physical Review E* **100**, 052604 (2019).
 - [29] N. Söker, S. Auschra, V. Holubec, K. Kroy, and F. Cichos, Active-particle polarization without alignment forces, arXiv:2010.15106 (2021), submitted to PRL.
 - [30] S. Auschra, N. Söker, V. Holubec, F. Cichos, and K. Kroy, Polarization-density patterns of active particles in motility gradients, arXiv:2010.16234 (2021), submitted to Phys. Rev. E.
 - [31] U. Erdmann, W. Ebeling, L. Schimansky-Geier, and F. Schweitzer, Brownian particles far from equilibrium, *The European Physical Journal B* **15**, 105–113 (2000).
 - [32] F. Schweitzer, *Brownian Agents and Active Particles* (Springer Berlin Heidelberg, 2007).
 - [33] P. Romanczuk, M. Bär, W. Ebeling, B. Lindner, and L. Schimansky-Geier, Active brownian particles, *The European Physical Journal Special Topics* **202**, 1–162 (2012).
 - [34] M. E. Cates and J. Tailleur, When are active brownian particles and run-and-tumble particles equivalent? consequences for motility-induced phase separation, *EPL (Europhysics Letters)* **101**, 20010 (2013).
 - [35] A. P. Solon, M. E. Cates, and J. Tailleur, Active brownian particles and run-and-tumble particles: A comparative study, *The European Physical Journal Special Topics* **224**, 1231–1262 (2015).
 - [36] S. Hermann and M. Schmidt, Active interface polarization as a state function, *Physical Review Research* **2**, 022003(R) (2020).
 - [37] N. A. Söker, *Heat driven Janus particles with spatially varying propulsion velocity*, Master's thesis, University of Leipzig (2018).
 - [38] N. Nikola, A. P. Solon, Y. Kafri, M. Kardar, J. Tailleur, and R. Voituriez, Active particles with soft and curved walls: Equation of state, ratchets, and instabilities, *Physical Review Letters* **117**, 098001 (2016).
 - [39] R. Wittmann, F. Smallenburg, and J. M. Brader, Pressure, surface tension, and curvature in active systems: A touch of equilibrium, *The Journal of Chemical Physics* **150**, 174908 (2019).
 - [40] Y. Fily, A. Baskaran, and M. F. Hagan, Dynamics and density distribution of strongly confined noninteracting nonaligning self-propelled particles in a nonconvex boundary, *Physical Review E* **91**, 012125 (2015).

- [41] H. Wioland, F. G. Woodhouse, J. Dunkel, J. O. Kessler, and R. E. Goldstein, Confinement stabilizes a bacterial suspension into a spiral vortex, *Physical Review Letters* **110**, 268102 (2013).
- [42] H.-J. Butt, K. Graf, and M. Kappl, *Physics and chemistry of interfaces* (John Wiley & Sons, 2013).
- [43] M. E. Cates, Diffusive transport without detailed balance in motile bacteria: Does microbiology need statistical physics?, *Reports on Progress in Physics* **75**, 042601 (2012).
- [44] R. Golestanian, Collective behavior of thermally active colloids, *Physical Review Letters* **108**, 038303 (2012).
- [45] E. Bertin, M. Droz, and G. Grégoire, Boltzmann and hydrodynamic description for self-propelled particles, *Physical Review E* **74**, 022101 (2006).
- [46] M. Abramowitz, *Handbook of mathematical functions, with formulas, graphs, and mathematical tables* (Dover Publications, New York, 1965).
- [47] H. Risken, *The Fokker-Planck Equation – Methods of Solution and Applications*, 2nd ed., edited by H. Haken (Springer-Verlag Berlin Heidelberg, 1989).
- [48] V. Holubec, K. Kroy, and S. Steffenoni, Physically consistent numerical solver for time-dependent fokker-planck equations, *Phys. Rev. E* **99**, 032117 (2019).
- [49] A. J. Rodenburg, *Thermodynamic Variables for Active Brownian Particles : Pressure, Surface Tension, and Chemical Potential*, Ph.D. thesis, Utrecht University (2020).
- [50] In the case of planar activity steps, the corresponding approximate moment equations, similar to Eqs. (17) and (18), could be mapped onto an exact one-dimensional run-and-tumble model of left or right-moving particles [30]. This 2-species model robustly captured the essential physics behind the formal results obtained for planar steps and justifies the large range of Péclet numbers over which the approximate moment equations [cf. Eqs. (17) and (18)] deliver accurate results. Since this equivalence between the two models is no longer present, deviations between approximate analytic and exact numerical results already occur for smaller Péclet numbers.
- [51]

$$\int_0^{2\pi} d\psi \cos \psi \int_0^\psi d\tilde{\psi} f(r, \tilde{\psi}) \sin \tilde{\psi} = \int_0^{2\pi} d\tilde{\psi} f(r, \tilde{\psi}) \sin \tilde{\psi} \int_{\tilde{\psi}}^{2\pi} d\psi \cos \psi$$

Appendix A: Polarization peak and density ratio

Within the active ($r < r_{\text{if}}$) and passive region ($r > r_{\text{if}}$) the general solution of the respective polarization and

density profiles read [Eqs. (22) and (23)]

$$p_a(r) = C_a I_1(r/\lambda_a), \quad \lambda_a = \left(\frac{D_r}{D} + \frac{v_0^2}{2D^2} \right)^{-1/2}, \quad (\text{A1})$$

$$p_p(r) = C_p K_1(r/\lambda_p), \quad \lambda_p = \sqrt{\frac{D}{D_r}}, \quad (\text{A2})$$

$$\rho_a(r) = \rho_a + \frac{C_a \lambda_a v_0}{D} [I_0(r/\lambda_a) - 1], \quad (\text{A3})$$

$$\rho_p(r) \equiv \rho_a(r_{\text{if}}) \equiv \rho_p = \text{const.}, \quad (\text{A4})$$

with $\rho_a \equiv \rho_a(0)$. The emerging integration constants C_a and C_p follow from the continuity conditions

$$p_p(r_{\text{if}}) = p_a(r_{\text{if}}), \quad p_a'(r_{\text{if}}) - p_p'(r_{\text{if}}) = \frac{v_0}{2D} \rho(r_{\text{if}}), \quad (\text{A5})$$

given Eqs. (25) and (26) in the main text. The first condition implies that

$$C_p = C_a \frac{I_1(r_{\text{if}}/\lambda_a)}{K_1(r_{\text{if}}/\lambda_p)}. \quad (\text{A6})$$

For the sake of brevity, we introduce the abbreviations $I_n \equiv I_n(r_{\text{if}}/\lambda_a)$ and $K_n \equiv K_n(r_{\text{if}}/\lambda_p)$. The second condition in Eq. (A5) yields

$$p_a' - p_p' = C_a \frac{I_0 + I_2}{2\lambda_a} + C_p \frac{K_0 + K_2}{2\lambda_p} = \frac{v_0}{2D} \rho_p \quad (\text{A7})$$

and using Eq. (A6) we get

$$\frac{C_a}{\rho_p} = \frac{v_0}{2D} \left(\frac{I_0 + I_2}{2\lambda_a} + \frac{I_1}{K_1} \frac{K_0 + K_2}{2\lambda_p} \right)^{-1}. \quad (\text{A8})$$

Knowing that the polarization peaks exactly at the interface (see Fig. 2), it follows from Eqs. (B1) and (B3) that the maximum relative polarization $p(r_{\text{if}})/\rho(r_{\text{if}})$ is given by $C_a I_1/\rho_p$. Using Eq. (A8) and introducing the geometry function (31),

$$G_A(r_{\text{if}}) = \left(\frac{I_0 + I_2}{2\lambda_a I_1} + \frac{K_0 + K_2}{2\lambda_p K_1} \right)^{-1}, \quad (\text{A9})$$

the maximum relative polarization reads

$$\frac{p(r_{\text{if}})}{\rho(r_{\text{if}})} = \frac{v_0}{2D} G_A(r_{\text{if}}), \quad (\text{A10})$$

as given in Eq. (29). The relative density profile, $(\rho - \rho_a)/\rho_p$, and thus also the bulk density ratio, ρ_p/ρ_a , can be obtained using Eqs. (B4), (B3), and (A8) and a similar approach.

Appendix B: Interior passive – Exterior active

We now consider the case where the particle is passive for $r < r_{\text{if}}$, and otherwise active. In analogy to the calculations in App. A one now has

$$p_p(r) = C_p I_1(r/\lambda_p), \quad (B1)$$

$$p_a(r) = C_a K_1(r/\lambda_a), \quad (B2)$$

$$\rho_p(r) \equiv \rho_a(r_{if}) \equiv \rho_p = \text{const.}, \quad (B3)$$

$$\rho_a(r) = \rho_p + \frac{C_a \lambda_a v_0}{D} [K_0(r_{if}/\lambda_a) - K_0(r/\lambda_a)]. \quad (B4)$$

Note that the argument of I_1 (K_1) now carries λ_p (λ_a) as characteristic length scale. Integration constants C_a and C_p are determined by the same continuity conditions (A5) as in App. A, yielding

$$C_p = C_a \frac{K_1(r_{if}/\lambda_a)}{I_1(r_{if}/\lambda_p)}, \quad (B5)$$

$$\frac{C_a}{\rho_p} = -\frac{v_0}{2D} \left(\frac{K_1}{I_1} \frac{I_0 + I_2}{2\lambda_p} + \frac{K_0 + K_2}{2\lambda_a} \right)^{-1}, \quad (B6)$$

where we used the abbreviations $I_n \equiv I_n(r_{if}/\lambda_p)$ and $K_n \equiv K_n(r_{if}/\lambda_a)$. Reduced density and polarization pro-

files, ρ/ρ_p and p/ρ_p , are plotted in Fig. 2 c) and d). Introducing the geometry function

$$G_P(r_{if}) \equiv \left(\frac{I_0 + I_2}{2\lambda_p I_1} + \frac{K_0 + K_2}{2\lambda_a K_1} \right)^{-1}, \quad (B7)$$

the (negative) polarization peak and the bulk density ratio are given by

$$\frac{p(r_{if})}{\rho(r_{if})} = -\frac{v_0}{2D} G_P(r_{if}), \quad (B8)$$

$$\frac{\rho_a}{\rho_p} = 1 - \frac{v_0^2 \lambda_a}{2D^2} G_P(r_{if}) \frac{K_0}{K_1}. \quad (B9)$$

Both quantities are plotted in Fig. 2 e) and f) (dotted lines). For $r_{if} \rightarrow \infty$, both approach their counterparts at straight planar active-passive interfaces [Eqs. (33) and (35)].